GMR
The Original

ECO-FRIENDLY SYNTHESIS OF FE-DOPED CAO NANOPARTICLES USING AEGLE MARMELOS LEAF EXTRACT AS A MULTIFUNCTIONAL PLATFORM FOR PHOTOCATALYTIC, ANTIMICROBIAL, AND ANTICANCER APPLICATIONS

Hardika Dave[1], Madhuresh Makavana[*2] Sarika Patel[3], Paras Patel[4]

[1]Department of Chemistry, Mehsana Urban Institute of Sciences, Ganpat University, Kherva, Mehsana, Gujarat- 384012
E-mail: hardidave5@gmail.com, ORCID ID: 0009-0006-0041-0802
[2*]Regional Forensic Science Laboratory, Vadodara, Gujarat- 390022, E-mail: madhuresh4n@yahoo.com, ORCID ID:0009-0007-0117-6234
[3]Department of Chemistry, Mehsana Urban Institute of Sciences, Ganpat University, Kherva, Mehsana, Gujarat-384012,
Email: spp04@ganpatuniversity.ac.in
[4]Department of Chemistry, Indus Institute of Sciences, Humanities & Liberal Studies (IISHLS), Indus University, Ahmedabad, Gujarat-382115, India, E-mail: paras12patel@yahoo.com paraspatel.gd@indusuni.ac.in, ORCID ID: 0000-0003-1896-5823

ABSTRACT
Water pollution from industrial sources continues to pose a serious threat to ecosystems worldwide, and the search for sustainable solutions has never been more pressing. This study explores the green synthesis of three nanoparticles (NPs) using Aegle marmelos (Bael) leaf extract as a natural reducing and stabilizing agent, namely calcium oxide nanoparticles (CaONPs), hematite nanoparticles (α-Fe_2O_3NPs), and iron-doped calcium oxide nanoparticles. The synthesized NPs were thoroughly characterized using UV-Visible spectroscopy, Fourier Transform Infrared Spectroscopy (FTIR), X-Ray Diffraction (XRD), Scanning Electron Microscopy (SEM), and Energy Dispersive X-Ray (EDX) analysis to confirm their structural, crystalline, and compositional properties. Photocatalytic degradation experiments were conducted on Reactive Red (RR), Reactive Blue (RB), and actual textile wastewater under solar irradiation and ultrasound treatment. Fe-doped CaONPs consistently outperformed the other two NPs in dye degradation, largely owing to their better charge separation efficiency and broader visible light harvesting capability. When screened for antimicrobial properties against Bacillus cereus, Micrococcus luteus, and Bacillus megaterium, Fe-doped CaONPs showed remarkable results, achieving full inhibition within just 18 hours. Additionally, cytotoxicity studies revealed noteworthy anticancer activity across all three NPs. Collectively, these results strongly suggest that Fe-doped CaONPs hold considerable promise as multifunctional nanomaterials for both environmental cleanup and biomedical use.

KEYWORDS: Green synthesis • Metal Oxide nanoparticles • Textile effluent remediation• Antimicrobial potential• Anticancer therapy.

INTRODUCTION
Water is one of Earth's most essential resources and plays a vital role in maintaining ecological balance and sustaining life. According to Indian scriptures, the Earth is blessed with five fundamental elements including soil, water, air, fire, and atmosphere, which collectively form the foundation of life [1]. Among them, water exhibits unique physical, chemical, and biological characteristics, making it essential for human survival and environmental sustainability [2,3]. However, recent rapid industrialization, urban expansion, and unsustainable agricultural practices have led to severe degradation of water quality [4,5]. Industrial discharge, from textile industries has introduced harmful pollutants such as synthetic dyes that became a serious threat to aquatic animals [6]. These contaminants not only threaten aquatic life but also lead serious health risks to humans [7,8]. Reactive Red dyes are widely used dying process because of its strong affinity towards fabric: however, substantial fraction remains free and discharge into water bodies. Due to their high stability and complex structure, Reactive Red dyes persist in water bodies for a long time. Their accumulation limit light penetration disturbs photosynthetic process, and degrade water quality. Conventional treatment methods are insufficient for complete dye degradation and may generate secondary contamination; To resolve these challenges, this study focus on green synthesis of NPs.
The urgency to address global water pollution as an increasing concern over dye-contaminated water, align with objectives of United Nations Sustainable Development Goals (UN SDG) 6, which emphasizes clean water and sanitation [9-12]. As highlighted in recent UN SDG reports, while some progress has been made such as 76% of wastewater in 73 countries receiving at least safe treatment by 2022 many water bodies still face significant threats due to deteriorating quality. Alarmingly, even in 2023, only 56% of water bodies across 120 countries were reported to be in good ecological condition [13]. Despite noticeable progress in wastewater treatment, a significant

proportion of water bodies continuous to be degraded due to textile industrial discharge. These trends signal a pressing need for innovative and sustainable solutions to restore and protect water quality worldwide [14]. In this context, the current work explores nano based catalytic system as an innovative approach for effective remediation of textile dye polluted water.

In this context, nanotechnology has emerged as a transformative tool, particularly through the synthesis and application of metal and metal oxide NPs [15]. NPs, characterized by their dimensions typically ranging from 1 to 100 nanometres, exhibit exceptional physicochemical properties such as high surface area-to-volume ratio, enhanced reactivity, and tuneable surface functionalities [16–18]. These features make them highly suitable for environmental remediation, especially in the degradation of complex organic pollutants present in wastewater. Among various metal oxides NPs, CaONPs, α-Fe_2O_3NPs, and Fe doped CaONPs have shown promising results due to their catalytic, antimicrobial, and eco-friendly characteristics.

This research adopts a green synthesis approach utilizing Aegle marmelos (Bael) leaf extract as a natural, renewable, and non-toxic reducing and stabilizing agent. The Aegle marmelos (Bael) leaf extract was selected due to its rich phytochemical compositions including flavonoids, phenolics and tannins which actively participate in metal ion reduction and nanoparticle stabilization during synthesis [19]. Moreover, the leaf extract of Aegle marmelos leaves have been widely reported to exhibit antioxidant, antimicrobial and catalytic potential making them suitable multifunctional NPs development [20]. The study focuses on synthesizing CaONPs, α-Fe_2O_3NPs, and Fe doped CaONPs and evaluating their efficiency in degrading hazardous dyes like RR and RB, as well as real textile wastewater. In addition to their catalytic roles, these NPs assessed for antimicrobial activities against bacterial strains such as Bacillus cereus, Micrococcus luteus, and Bacillus megaterium, thereby extending their potential applications to the biomedical field.

This investigation aims to contribute to the development of cost-effective, scalable, and environmentally benign nanomaterials that can address critical water pollution challenges while aligning with the principles of sustainable development and green chemistry.

MATERIALS AND METHODOLOGY:

Table1. The details of materials, including grade, supplier and purification method

Sr. No	Material/Chemical	Chemical Formula	Grade	Supplier	Purification Method
1	Aeglemarmelos leaves	-	Fresh plant material	Local region	Washed with distilled water and shade dried
2	Calcium Nitrate Tetrahydrate	$Ca(NO_3)_2 \cdot 4H_2O$	AR Grade	Merck/sigma Aldrich/SRL	Used as received
3	Ferric Chloride	FeCl3	AR Grade	Merck/sigma Aldrich/SRL	Used as received
4	Sodium Hydroxide	NaOH	AR Grade	Merck/sigma Aldrich/SRL	Used as received
5	Distilled water	H2O	LR Grade	In-House	Double distillation
6	Potassium Bromide	KBr	Spectroscopic Grade	Merck/sigma Aldrich/SRL	Grinding using Mortar and pestle (non porus)

2.1. Materials:

Fresh and mature leaves of Aegle marmelos collected from local region and used for extract preparation. Calcium nitrate tetrahydrate ($Ca(NO_3)_2 \cdot 4H_2O$), Ferric chloride ($FeCl_3$) of AR grade were obtained from a reliable chemical supplier, used as the precursors for the synthesis of CaONPs, α-Fe_2O_3NPs and Fe doped CaONPs, Sodium hydroxide (NaOH) was used as the precipitating agent to maintain basic conditions. The details of materials, including grade, supplier and purification method are mentioned in Table 1.

2.2. Methodology:

2.2.1. Preparation of Aegle marmelos leaf Extract:

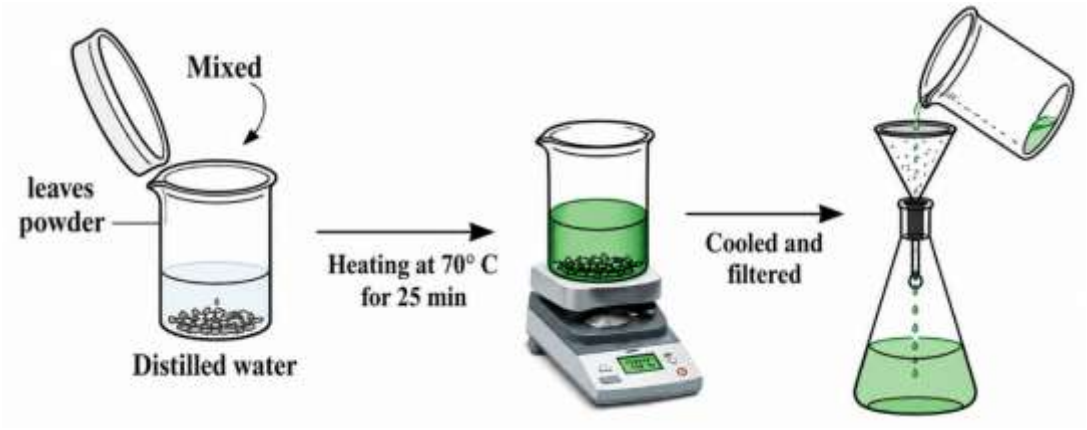

Figure 1. Preparation of Aegle Marmelos leaves extract

Fresh leaves of Aegle marmelos were cleaned with distilled water and dried at ambient temperature away from direct sunlight. The stepwise procedure for preparation of Aegle Marmelos leaves extract is shown in Figure 1. The dried leaves were finely powdered using a mechanical grinder. To prepare the extract, 5 grams of leaf powder were mixed with 100 mL of distilled water and heated at 70°C for 25 minutes under continuous stirring. After that, the mixture was cooled and filtered using Whatman No. 1 filter paper to remove solid residues. The resulting filtrate was stored at 4°C for further use in NPs synthesis.

2.2.2. Synthesis of Calcium oxide Nanoparticles (CaONPs):

Figure 2. Synthesis of Calcium Oxide nanoparticles (CaONPs).

To synthesize CaONPs, a 0.001 M aqueous solution of Ca(NO3)2.4H2O was prepared. Then, 40 mL of freshly prepared Aegle marmelos extract was added dropwise under gentle stirring at room temperature as shown in Figure 2. The mixture was stirred continuously for 2 hours at a temperature range of 25–35°C. After thorough mixing, 0.2 N NaOH was added dropwise to adjust the pH to basic conditions, facilitating the precipitation of NPs. The reaction mixture was then centrifuged at 3500 RPM for 20 minutes. The obtained precipitate was washed several times with distilled water to remove unreacted substances and dried in a hot-air oven for further characterization.

2.2.3. Synthesis of Hematite Nanoparticles (α-Fe_2O_3NPs):

Figure 3. Synthesis of Hematite nanoparticles (α-Fe_2O_3NPs)

A 0.01 M solution of FeCl3 was prepared in distilled water. As mentioned in Figure 3., 40 mL of Aegle marmelos leaf extract was gradually added under constant stirring. The pH of the solution was adjusted to basic by slowly adding 0.2 N NaOH dropwise. The reaction mixture was maintained at a temperature of 25–30°C and stirred for 2 hours. After the reaction, the mixture was centrifuged at 3500 RPM for 30 minutes to isolate the formed α-Fe_2O_3NPs. The NPs were washed repeatedly with distilled water and ethanol to eliminate any impurities. The purified sample was dried at controlled temperature and stored for further analysis.

2.2.4. Synthesis of Iron doped Calcium oxide nanoparticles (Fe doped CaONPs):

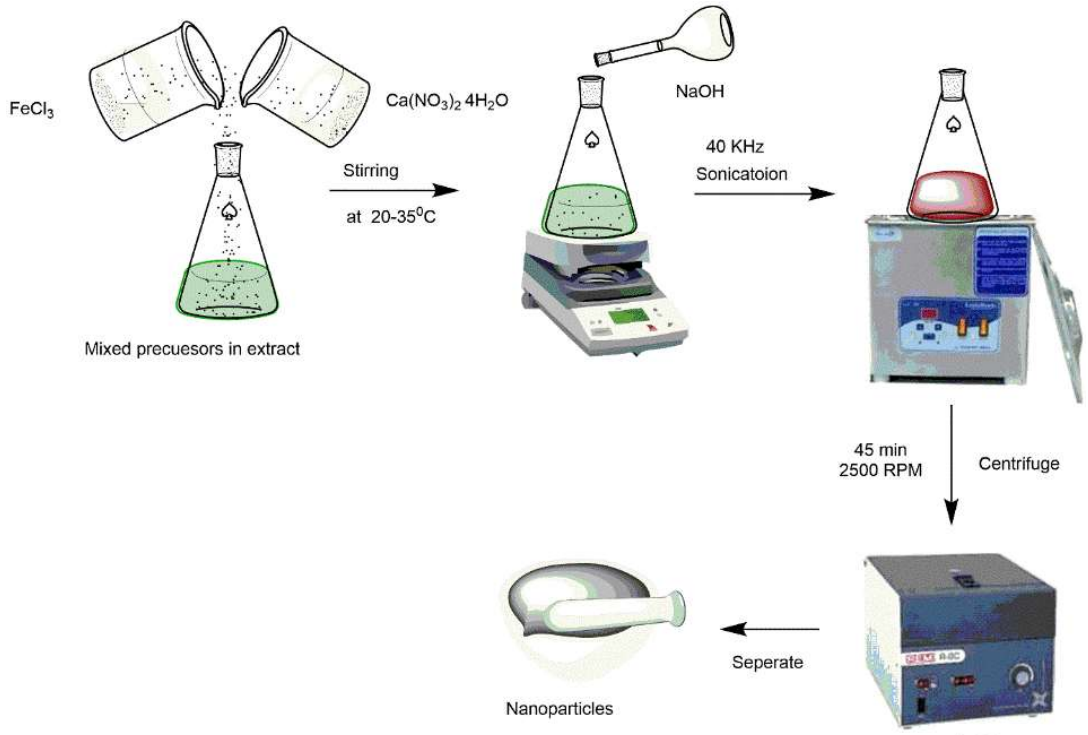

Figure 4. Synthesis of Iron doped Calcium oxide nanoparticles (Fe doped CaONPs).

For Fe doped CaONPs synthesis, as shown in Figure 4. 80 ml of 0.003M FeCl3 solution and 20 ml 0.001M Ca(NO3)2 solutions were mixed. Subsequently, 40 ml of Aegle marmelos leaf extract was added to the mixture. To maintain the basic nature, 0.2 M NaOH solution was added dropwise manner, stirred at 45-500 0C for 2-3 hours, and then applied to the ultra- sonication treatment at a frequency of 40 kHz for 30 minutes to achieve better dispersion medium. After sonication, the solution was centrifuged at 4500 RPM for 45 minutes. The resulting precipitates was collected, washed several times with distilled water, dried and stored in refrigerator for further characterization.

2.2.5. UV-Visible spectrophotometric analysis:
The NPs were analyzed using a Shimadzu UV-Visible spectrophotometer with UV-Probe software at an operating range of 200-800 nm with a 1 nm resolution. The NPs were suspended in distilled water and then subjected to ultrasonic bath for homogenization. The samples were put into quartz cuvettes, with distilled water used as the blank for baseline corrections. The characteristic absorption peak confirmed the formation and optical properties of the NPs [21–23].

2.2.6. FT-IR spectroscopic analysis:
The FT-IR analysis was done with a Bruker FT-IR spectrophotometer, within the range of 4000 – 400 cm^{-1}. For the pellet preparation, a sample of dried NPs and a large excess of KBr in approximate ratio of 1:100 was mixed then ground so that they were as homogeneous as possible. Then, the resulting mixture was loaded into the hydraulic press and pressed into a transparent pellet at room temperature at a high pressure. After this step, the formed pellet was then immediately analyzed for obtaining the FT-IR spectrum with the resultant peaks used to determine the presence of the functional groups and the metal-oxygen bonding[23, 24].

2.2.7. XRD analysis:

The diffraction pattern of the NPs was evaluated using XRD analysis performed with the Bruker D8 Discover Instrument Smith B with X-ray tube radiation Cu-Kα (λ = 1.54 Å) operated at 40 kV and 30 mA. The sample was prepared by grinding the dried NPS powder to a fine powder and evenly distributing it across a piece of clean sample holder material to achieve smooth and uniform surfaces upon which testing for the detection of X-ray diffraction patterns could occur. The sample was then scanned through an angular range of 2θ from 10 to 80 degrees with an appropriate scanning rate. Based on the XRD patterns, the NPs were evaluated for crystalline size using the following Scherrer equation no. 1[25, 26].

$$D = \frac{\kappa\lambda}{\beta\cos\theta} \quad \ldots(1)$$

Here, D represents the average crystallite size, typically expressed in nanometres. The constant k, known as the Scherrer constant, depends on the shape of the crystallites and is usually taken as 0.9. The term λ is the wavelength of the X-ray radiation used in the diffraction experiment. The parameter β refers to the line broadening at full width at half maximum (FWHM) of the diffraction peak, measured in radians. Finally, θ is the Bragg angle, which is equal to half of the measured diffraction angle (2θ). This equation is widely used in X-ray diffraction analysis to estimate the size of nanocrystalline materials.

2.2.8. SEM with EDX analysis:

The surface morphology was studied using JEOL JSM-7900F SEM operated at accelerating voltages of 10–20 kV [27,28]. An aliquot of the dry sample was lightly dusted onto a piece of conductive carbon tape on an aluminium stub, then sputter-coated with a very thin layer of gold to increase conductivity and reduce charging. The sample was then placed into the SEM chamber and high magnification images were taken at varying levels for both morphology and surface characteristics. Elemental composition was analysed by EDX in combination with SEM. While collecting images of the sample the EDX utilised to detect the characteristic X-rays emitted from the sample, enabling the qualitative and quantitative analysis of the constituent elements to be examined. Both techniques provided extensive information regarding the morphology and elemental composition of the synthesised NPs.[29–31].

2.2.9 Photocatalytic dye degradation:

The dye degradation study was carried out to evaluate the catalytic efficiency of green-synthesized NPs for the removal of organic dye pollutants from aqueous solutions. A known concentration of dye solution, including RR, RB, and a Real wastewater sample collected from Mafatlal Textile Industry, was prepared and treated with CaONPs, α-Fe_2O_3NPs, and Fe doped CaONPs under controlled conditions. The experiments were performed using two different approaches: in Method 1, the reaction mixture was subjected to one-time sonication for 15 minutes followed by solar irradiation at regular intervals of 15 minutes, while in Method 2, sonication and solar irradiation were applied alternately at the same time intervals. The degradation process was monitored by recording the decrease in absorbance at the characteristic λmax using a UV–Visible spectrophotometer, and the efficiency was evaluated by calculating the normalized concentration ratio (C/C_0) over time using following the equation no 2.

% of Degradation Efficiency

$$= 1 - \left({}^{C}/_{C_0}\right) * 10 \quad \ldots(2)$$

Here, C_0represents the initial concentration of the substance at the starting time, while C denotes the concentration of the substance at a specific time t. This relationship is commonly used to track how the concentration of a substance changes over time during a reaction or process.

2.2.10. Antimicrobial Activity:

The antimicrobial efficiency of the synthesized NPs was evaluated by measuring the zone of inhibition utilizing the method of agar well diffusion. To conduct this, sterile nutrient agar plates were prepared and uniformly inoculated with microbial cultures Micrococcus luteus, Bacillus cereus and Bacillus megaterium that have been recently grown using a sterile cotton swab. Approximately 6 mm diameter wells are created in the agar with a sterile cork borer, and a preset amount of nanoparticle suspension is applied into the wells at various concentrations. The plates are incubated at 37 °C for 24 hours and then at 28–30 °C for 48 hours for bacterial strains and fungal strains, respectively, after which time the formed inhibition zones are measured in mm using a ruler or a digital calliper and evaluated for antimicrobial activity based on the size of the inhibition zones, i.e. how effective the NPs are ainhibiting the growth of specific microorganisms that were tested.

2.2.11. Anticancer Activity:

In this study, MCF-7cell line in Dulbecco's Modified Eagle Medium (DMEM) (enriched with 10% fetal bovine serum, 1 % Antibiotic- Antimycotic) was used. Cells were seeded such that to reach 50,000 cells/well. Cells were maintained at 37°C under an atmosphere of 5% CO2. After 24 hours, different concentrations (100 µg/ml, 50 µg/ml, 25 µg/ml, 12.5 µg/ml, 6.25µg/ml, 3.12 µg/ml, 1.56 µg/ml & 0.78 µg/ml) of the given sample was added to each well. Then after 18-20 hours of incubation, activity of the given sample was tested by MTT assay. Whole experiment was done in triplicates.

2.2.11.1. MTT Assay:

MTT test was used to evaluate substrate toxicity. MTT [3-(4,5-dimethylthiazol- 2yl)-2,5] diphenyltetrazolium bromide; thiazolyl blue] is transformed by mitochondrial dehydrogenases into formazan, enabling mitochondrial activity and cell viability to be assessed. A 100 µL aliquot of MTT solution was added to each well. After 4h incubation in a CO2

atmosphere, the supernatant was removed and the formazan crystals were dissolved by adding 100 µL of dimethyl sulfoxide (DMSO) to each well. After shaking for 10 min, absorption was measured at 570 nm using a microplate reader. Results were expressed as corrected optical densities (OD).

RESULTS AND DISCUSSION

UV-Visible Spectrophotometry Analysis:

To confirm the successful synthesis and evalute the properties of green synthesized NPs, many analytical techniques were employed. UV- Visible spectroscopy was used to study optical properties and confirm the synthesis of NPs through characteristic absorbance peak[19, 20].

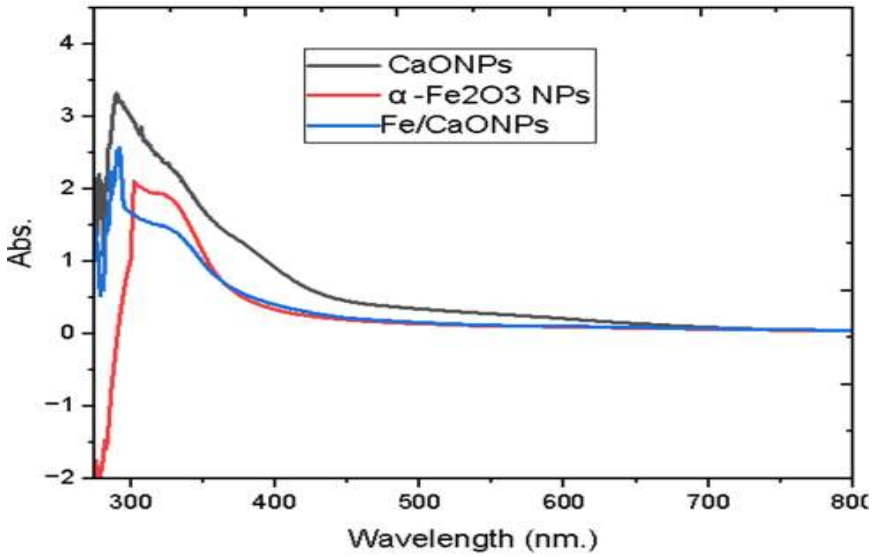

Figure 5. UV-Visible Spectrophotometry Analysis of NPs.

The UV-visible absorption spectrum of CaONPs as shown in Figure 5. exhibited a sharp peak in the range of 280-320 nm [32–34]. This peak is attributed to electronic transition in Ca-O bond and confirms the formation of CaONPs. The intensity of peak suggests relatively uniform particle size and minimal agglomeration. In Case of α-Fe_2O_3NPs in Figure 5. revealed a broader α-Fe_2O_3NPs peak in the range of 380-450 nm [35–37]. This region is corresponding to the ligand-to-metal charge transfer (LMCT) transitions from O^{2-} to Fe^{3+} ions. The observed spectrum is consistent with previously reported optical behaviour of iron oxide and indicates the successful formation of α-Fe_2O_3NPs [37–40]. The UV-Vis analysis of Fe doped CaONPs as shown in Figure 5. demonstrated a broadened and red-shifted absorption band ranging from approximately 320 to 450 nm. This shift in the absorption maximum, relative to both CaONPs and α-Fe_2O_3NPs, is indicative of electronic interaction and structural modification due to iron doping into the CaONPs. The broad nature of the peak suggests an altered bandgap energy, which enhances the material's potential for photocatalytic and environmental applications [43].

FT-IR spectrophotometric analysis:

FT-IR spectrophotometric analysis technique confirmed the reliable analysis of phytochemicals interactions as well as confirmation of characteristic metal oxygen bond formation in green synthesized NPs.

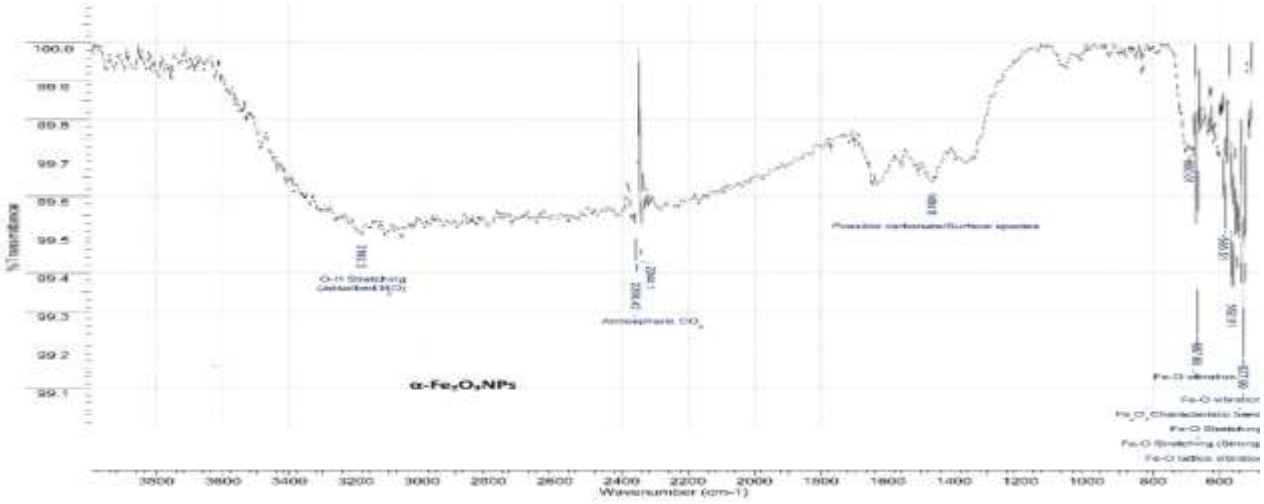

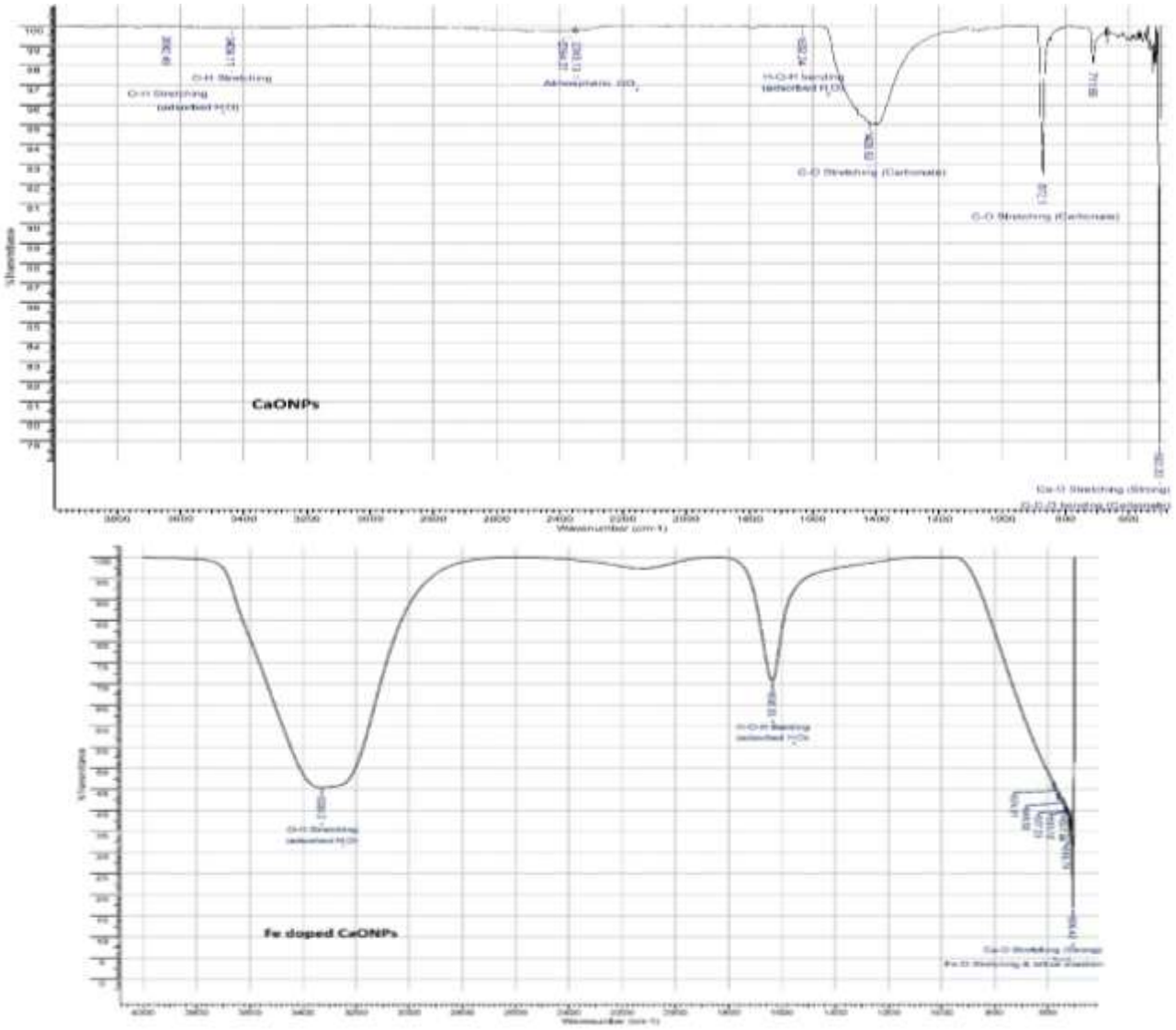

Figure 6. FT-IR Spectrophotometry Analysis of NPs.

The FT-IR spectrum of green synthesized CaONPs Shown in Figure 6. reveals characteristic absorption bands that show both formation metal-oxygen bond and involvement of phytochemicals. At about ~3182 cm^{-1}, a broad absorption band indicates the presence of O-H stretching vibrations caused by absorbed water molecules (also known as hydroxyl groups). The peak at ~2343 cm^{-1} is due to atmospheric CO_2 content. A peak at approximately ~1484 cm^{-1} indicates that a carbonate ion is formed on the surface; thus,h CaONPs likely contain carbonate materials. Two additional prominent bands at approximately ~687 and ~527 cm^{-1} represent the Ca-O stretching vibrations which confirms that CaONPs were generated. In the FT-IR spectrum of α-Fe_2O_3NPs, characteristic absorption bands appear between 503 - 600 cm^{-1} and correlate well with the stretching band of Fe-O bonds confirming that iron oxide NPs had been synthesized successfully and match previously published FT-IR data [44, 45]. In the case of Fe doped CaONPs, the spectrum shows absorption bands between ~530 - 580 cm^{-1} indicating the presence of both Ca-O and Fe-O overlaps that results from the incorporation of iron into CaO's crystal structure. These Peak shifts, along with Peak width can be used as evidence for the successful addition of iron to the CaO crystal structure. Overall, the FT-IR data supports the identification of the synthesis of CaONPs, α-Fe_2O_3NPs and Fe doped CaO NPs, and while also highlighting the role of phytochemicals from Aegle marmelos leaf extract in the reduction and stabilization process [25, 34, 42, 43, 48].

XRD analysis:

The X-ray diffraction patterns of CaONPs, α-Fe_2O_3NPs and Fe doped CaO NPs are shown in Figure 7. The XRD analysis was used to determine crystallite size of NPs.

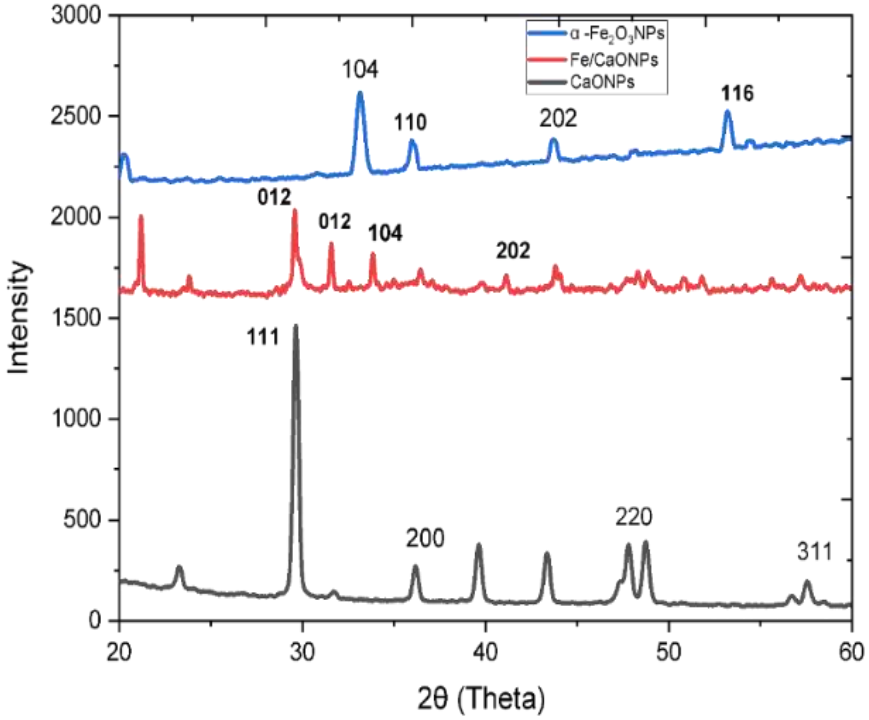

Figure 7. XRD Analysis of NPs.

The diffraction pattern of CaONPs, α-Fe_2O_3NPs and Fe doped CaO NPs presented in Fig.7. The XRD pattern of CaONPs exhibit sharp and intense peaks at 2θ values around 320, 370, 540 and 640, which correspond to the standard cubic shape of CaONPs according to (Joint Committee on Powder Diffraction Standards) JCPDS database no. 00-037-1497 [31, 47, 48]. The well-defined nature of these peaks suggests high crystallinity and purity. The absence of additional peaks confirm that no impurity was formed during the synthesis. The intense peak indicate that the particle size 22.72 in narrow scale range, which can be further calculated by using Scherrer equation No. 1 [51].

In the case of α-Fe_2O_3NPs, the XRD pattern shows several peaks around 24.1, 33.2, 35.6, 40.8, 49.5 and 54.1, which are characteristic of rhombohedral hematite structure according to JCPDS standard, database no. 01-072-6226 [49, 50]. The presence of the peaks confirms the successful synthesis of pure α-Fe_2O_3NPs. The moderate intensity of peaks indicate the crystalline size 8.84 nm, which can further calculated using Scherrer equation [51]. The XRD pattern of Fe doped CaO NPs in blue graph shows a combination of diffraction peak from both phase of CaONPs and α-Fe_2O_3NPs. While the dominant peaks of CaONPs are retained, and weaker peaks corresponding to iron oxide are also present. Especially, some of the CaONPs peaks exhibit slight shift in position and broadening effect, which is indicative of lattice distortion caused by the incorporation of Fe+3 ions into the CaONPs. This observation confirms the successful doping of iron within CaONPs. The broadening of peaks may also point toward a reduction in crystalline size or increased structural disorder due to doping[54]. The crystalline size of Fe doped CaONPs is 9.14 nm.

SEM with EDX analysis:

SEM and EDX analysis was employed to investigate the morphology and elemental composition of new synthesized NPs likewise CaONPs and Fe doped CaONPs [54]. This dual characterization provides insights into surface texture and purity of element present in each sample.

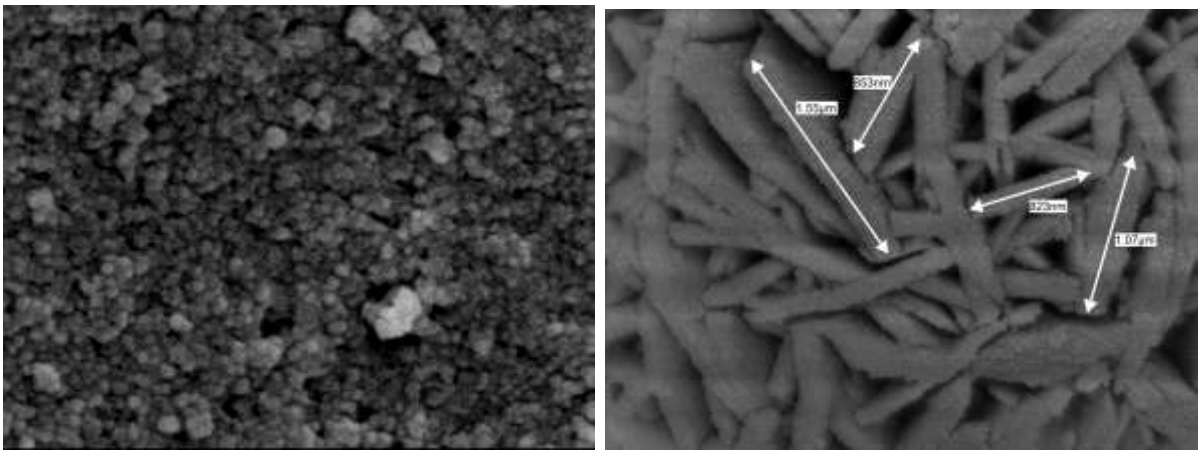

Figure 8. SEM analysis of (1)CaONPs and (2) Fe doped CaO NPs

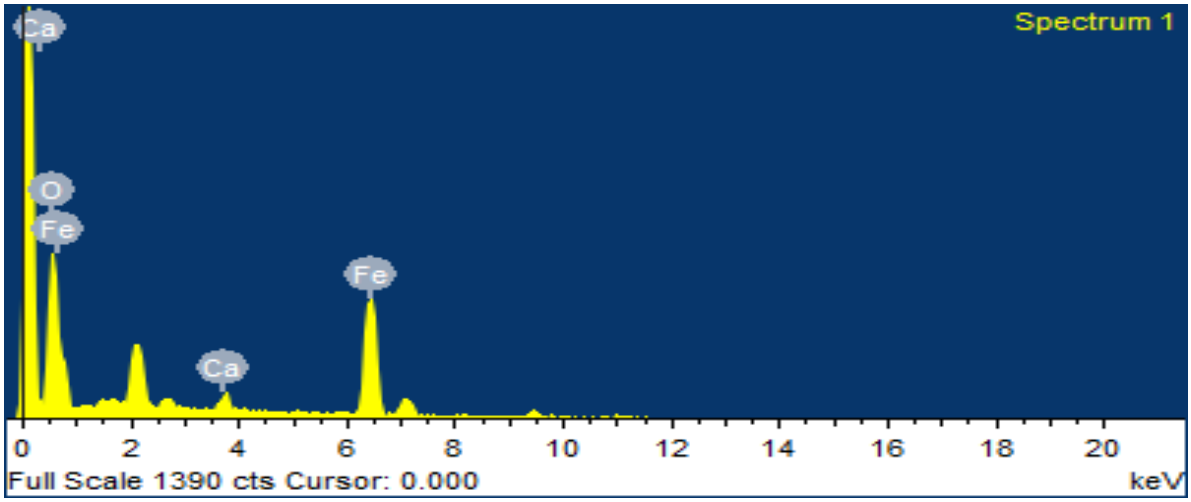

Figure 9. EDX analysis of CaONPs and Fe doped CaO NPs

This characterization provides insights into surface morphology and purity of element present in each sample. The SEM image of CaONPs in Figure 8 (1). revealed particle with spherical morphology, which is typical of green synthesized NPs due to the presence of bioorganic stabilizing agent. The average particle size was observed to be in the range of 40-70 nm, suggesting good dispersion under mild synthesis conditions [50]. The SEM image of Fe doped CaONPs in Figure 8 (2). displayed a more heterogeneous morphology, with better dispersion than CaONPs and α-Fe_2O_3NPs[55]. The surface texture appeared finely granular, and particles showed less agglomeration because of ultrasonicator treatment during the synthesis. The doping of Fe on CaONPs may have disrupted particles growth, resulting in smaller and uniform structures [56]. The EDX spectrum shown in Figure 9. confirmed the Calcium (Ca), Iron (Fe), and Oxygen (O) as major constituents, clearly indicating the successful formation of Fe doped CaONPs [54]. The absence of impurity peaks further validates the purity of synthesized NPs. The SEM with EDX analysis together confirms that all three NPs were successfully synthesized with nanoscale morphology and high elemental purity. The Fe doping on CaONPs altered both morphology and composition, yielding smaller, better dispersed particles, which is beneficial for catalytic and biological applications [39, 54].

The successful synthesis was confirmed through UV-Visible, FT-IR, XRD and SEM-EDX analyses, all of which demonstrated pure NPs with well-defined morphology and composition. The presence of bioorganic functional groups on the NPs surface further highlights the role of phytochemicals in controlling particle growth stability, making this a valuable green alternative to conventional chemical synthesis methods.

Photocatalytic dye degradation applications:

The green synthesized NPs exhibit unique physicochemical properties such as high surface area, enhanced crystallinity and tuneable optical behaviour making them suitable for a wide range of technological and wide range of environmental applications. Due to their biocompatibility and catalytic efficiency, these NPs hold significant application in multidisciplinary section[58].

Figure 10. Reaction mechanism of photocatalytic dye degradation

The photocatalytic degradation is an effective and eco-friendly technique used to treat dye contaminated wastewater, as shown in Figure 10., this method involves the use of photocatalyst such as metal oxide and metal doped metal oxides upon light irradiation, generate reactive species like hydroxyl radicals (•OH) and super oxide radicals ($O_2^{\bullet -}$). These species breakdown complex dye molecules in to simpler nontoxic compounds like CO2 and H2O [60] .

When the photocatalyst is exposed to UV or visible light, electrons in the valence band become excited and move to the conduction band, leaving behind holes in the valence band, these electron- hole pair then interact with water and oxygen present in environment to produce ROS (Reactive Oxygen Species), which attack dye molecule and degrade them [60]

The degradation efficiency can be further enhanced by modifying the photocatalyst through metal or non-metal doping, combining them with other process like ultra-sonication or solar irradiation, For example, Fe doped photocatalyst showed improved charge separation and extended light absorption in the visible range, thus improving degradation rates under sunlight [58, 59]. Moreover, this method was influenced by several factors including the type and concentration of dye, catalyst dosage, pH of solution and type of irradiation used Recent studies have also highlighted the importance of combining Photocatalysis with ultrasonic treatment, which enhance cavitation and helps to disperse dye molecule more effectively across the catalyst surface [63].

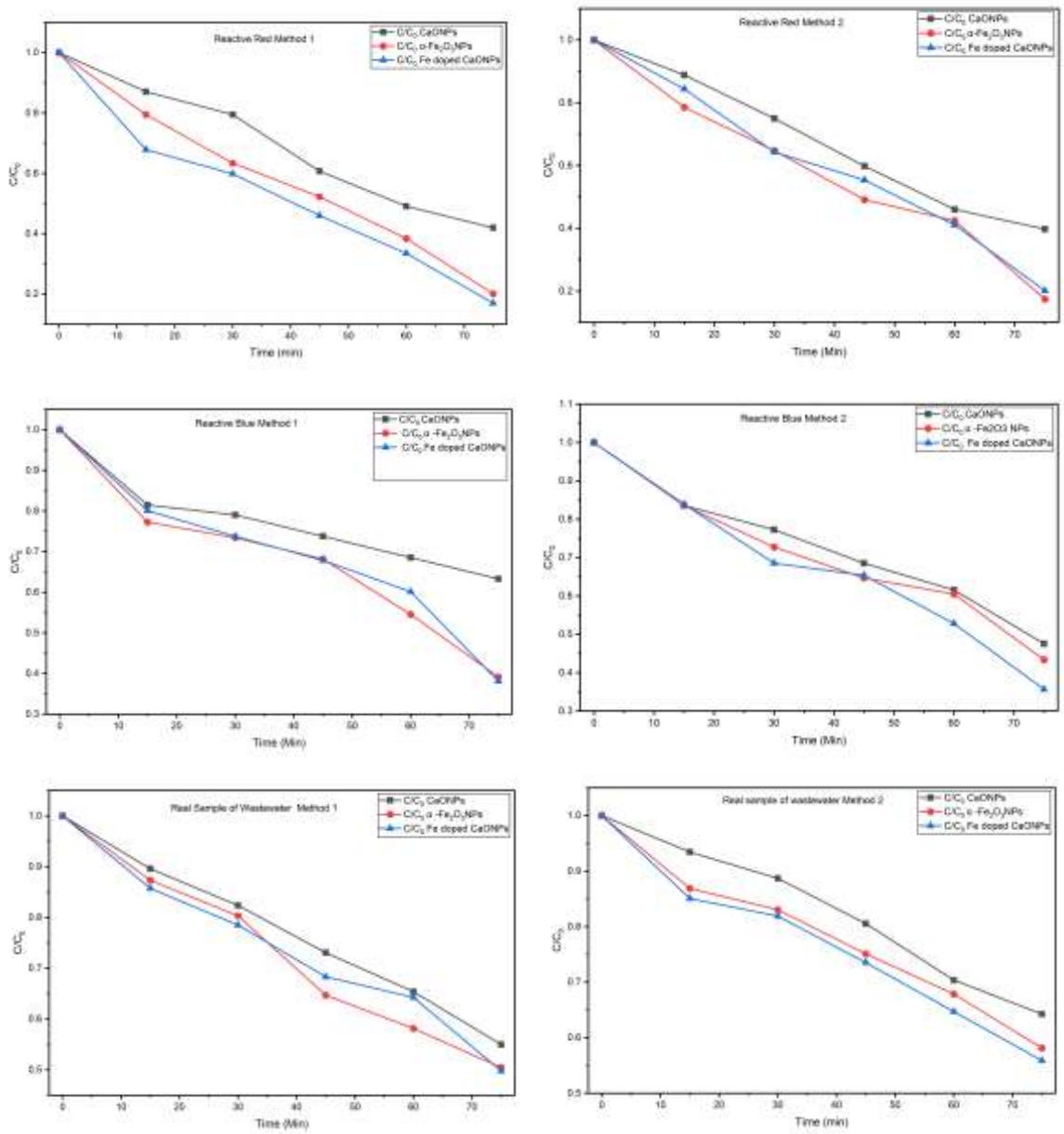

Figure 11. Photocatalytic dye degradation using green synthesized NPs

As shown in figure 11. for Reactive Red dye degradation under method 1, Fe doped CaONPs exhibited the highest degradation efficiency as 83.03% followed by α-Fe_2O_3NPs as 79.91%, while CaONPs showed the lowest efficiency with 58.03%. The better efficiency of Fe doped CaONPs can be attributed to the enhanced charge separation and broader light absorption due to Fe doping. The improvement is likely due to increased mobility of charge carriers. When applied to method 2, α-Fe_2O_3NPs performed better than Fe doped CaONPs, showing a degradation efficiency of 82.58% compared to 79.91 because of improved cavitation and dispersion effects under alternating solar and ultrasonic condition. However, CaONPs remained least effective as 60.26% possibly due to fewer active photocatalytic sites.

For Reactive Blue dye under Method 1, Fe doped CaONPs again demonstrated the better efficiency of 61.88%, closely followed by α-Fe_2O_3NPs showed degradation efficiency as 60.83%. CaONPs showed considerably lower efficiency as 36.71%, reinforcing the need for surface modification or doping to enhance visible light response. Using method 2, the degradation efficiencies of all photocatalyst increased. Fe doped CaONPs achieved 66.56%, α-Fe_2O_3NPs reached 64.83% and CaONPs showed moderate improvement to 41.44% because of ultrasound induced catalyst dispersion, which accelerates degradation kinetics.

The catalyst also treated against real textile effluent obtained from local textile industries. In method 1, Fe doped CaONPs once again demonstrated the highest degradation efficiency of 77.17% than α-Fe_2O_3NPs and CaONPs shown degradation

efficiency as 73.61% and 41.03% respectively. In method 2, all three types of NPs showed better photolytic activity. Fe doped CaONPs gave the highest dye degradation at 83.63%, followed by α-Fe_2O_3NPs with 80.73% and CaONPs with 57.71%. This improvement is likely due to the combined effect of sunlight and ultrasonic waves, which helped dye molecules to reach the catalyst surface more easily and improved the breakdown of pollutant in water. Hence, Fe doped CaONPs showed the good dye degradation for all including Reactive Red, Reactive Blue dye as well as real sample of wastewater. This is because doping of Iron on CaONPs improves sunlight adsorption and help in keep the charges separated longer, leading to better photocatalytic action, α-Fe_2O_3NPs also worked well, especially in method 2, due to good response to visible light and ultrasound. However, their performance was slightly lower than Fe doped CaONPs because of some charge loss. CaONPs showed the lowest activity, as have faster charger recombination.

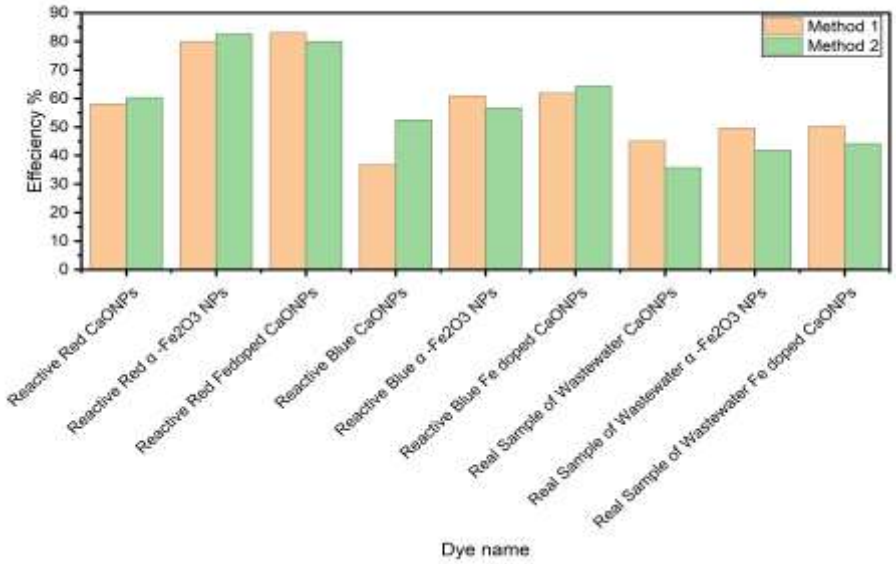

Figure 12. photocatalytic dye degradation using CaONPs, α-Fe_2O_3NPs and Fe/CaONPs under two different methods

The comparative graphical representation Figure 12. shown photocatalytic dye degradation using CaONPs, α-Fe_2O_3NPs and Fe doped CaONPs under two different methods.

Kinetic investigation of photocatalytic dye degradation:

Photocatalytic degradation of dyes often follows pseudo-first-order kinetics, particularly when the dye concentration is low and the concentration of catalyst remain constant. The degradation rate is described using the Langmuir-Hinshelwood model, simplified to the first-order equation No 3. as follows [64].

$$\ln\left(\frac{C}{C0}\right) = kt \qquad \ldots (3)$$

The kinetic investigation of dye degradation was used to studied using pseudo first order kinetics. The linearity of $\ln C/C0$ vs. time plots and corresponding to R2 values indicate how well the degradation take place.

Among the three NPs, Fe doped CaONPs exhibited the highest rate constant (k) and regression values for all dyes. For example, in RR dye, Method 1 showed R2 value of 0.98 with a rate constant of 0.018 min-1, in Method R2 was 0.91 with k= 0.019 min-1. This implies that Fe doped CaONPs maintained consistent degradation performance across both methods. α-Fe_2O_3NPs also demonstrated good kinetics. For RR dye, the rate constant in Method 1 was 0.017 min-1 with R2 of 0.98, while in Method 2 is slightly increased to 0.020 min-1, through R2 dropped to 0.89. This suggests slight decreases in linearity but a faster reaction rate under Method 2. On the other hand, CaONPs showed relatively lower rate constants and R2 values, especially for RB dye, where Method 1 showed R2 =0.93 and rate constant k = 0.005 min-1, and in Method 2 showed R2 = 0.96 with k = 0.009 min-1. This lower performance may be attributed to rapid charge combination and limited light absorption. For the real sample of waste water, all catalysts performed better in Method 1. Fe doped CaONPs achieved R2 of 0.96 and rate constant k = 0.008 min-1, while. α-Fe_2O_3NPs showed the highest R2 = 0.99 with k = 0.009 min-1. This highlights the reliability of α-Fe_2O_3NPs for complex wastewater pollutants.

Hence, Fe doped CaONPs proved to be the most effective photocatalyst for degrading RR and RB as well as real sample of textile wastewater under both solar and Sonicator treatment, due to enhanced charge separation, broader light absorption and improved charge carrier mobility from Fe doping. α-Fe_2O_3NPs showing comparable absorption especially in alternating solar-ultrasonic conditions, owing to strong visible light response and cavitation effects, while CaONPs remained least effective because of rapid recombination, through ultrasound moderately improved their activity. Kinetic studies confirmed pseudo-first order behaviour, with Fe doped CaONPs exhibiting the highest rate constant and R2 values, followed closely by α-Fe_2O_3NPs, making Fe doped CaONPs the most reliable choice for efficient dye contaminated wastewater treatment.

Antimicrobial Activity:

An antimicrobial activity can be attributed to multiple mechanisms. Metal oxide NPs are known to generate reactive oxygen species (ROS) such as hydroxyl radicals and super oxide anions, which disrupts bacterial cell membranes, proteins and nucleic acids as shown in Figure 13. In addition, the NPs can interact with negatively charged bacterial cell wall,

leading to membrane damage and leakage of cellular contents. Fe doping on CaONPs may further enhance electron transfer processes, thereby increasing ROS production and bacterial action [65].

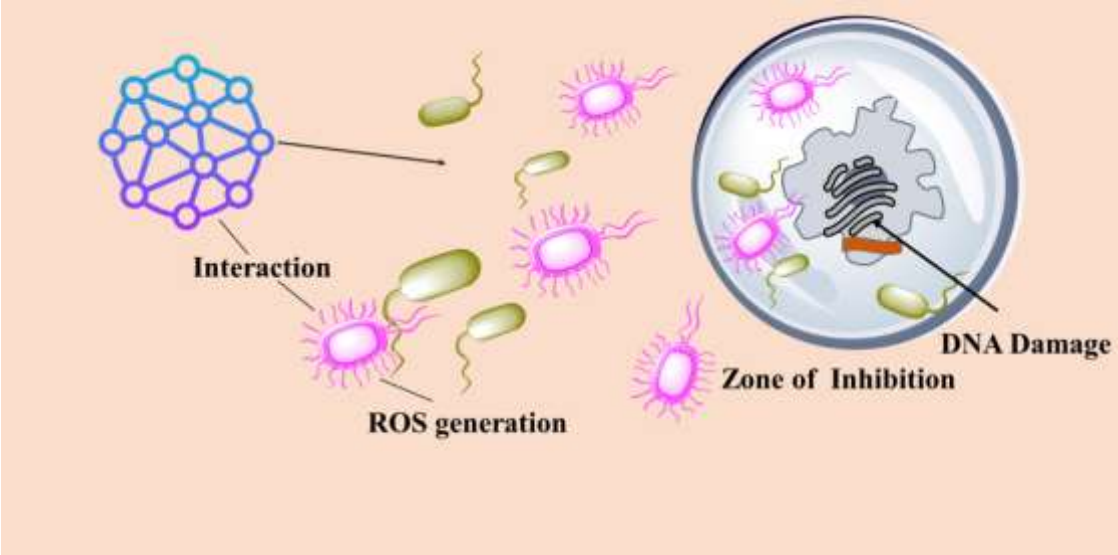

Figure 13. Mechanism of antimicrobial potential

The antimicrobial potential of green synthesized Fe doped CaONPs at different concentration of 25, 75, and 100 µg/ml were evaluated using agar well diffusion method against selected bacterial strains including Micrococcus luteus, Bacillus cereus and Bacillus megaterium. The fresh bacterial cultures were prepared in nutrient broth and incubated at 370 C for 18 to 20 hours.

According to the results observed in Figure 14., where the zone of inhibition around the well indicates the potential antimicrobial activity of NPs. Based on the observations, the antimicrobial activity of Fe doped CaONPs was concentration dependent, with higher concentrations showing greater antimicrobial effects. At the lowest concentration of 25 µg/ml.

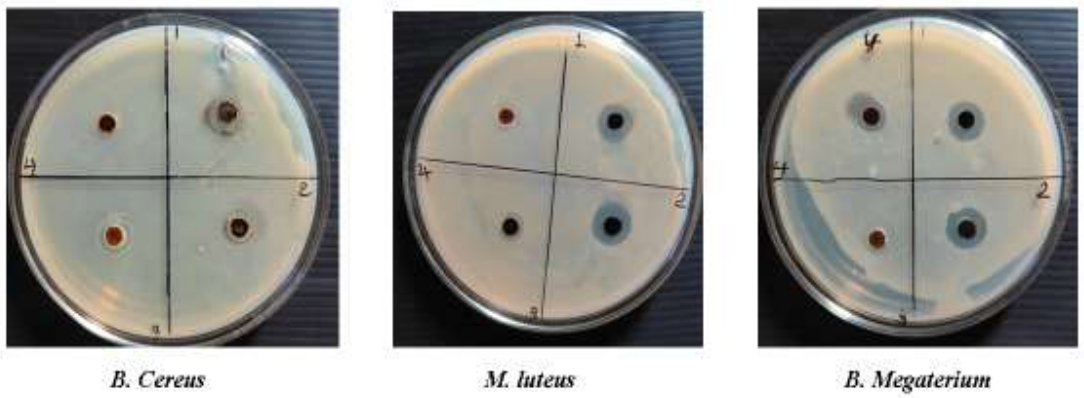

Figure 14. Antimicrobial application of green synthesized NPs

The higher susceptibility of gram-positive bacteria as M. luteus and B. cereus compared to B. megaterium suggest that structural difference in bacterial cell walls influence nanoparticle activity. The results are consistent with earlier reported CaO and Fe doped metal nanoparticle demonstrating significant antimicrobial potential [63,64]

Anticancer activity:

The concentration-dependent decrease in viability may be attributed to mechanisms commonly associated with metal oxide NPs, such as induction of ROS, oxidative stress, mitochondrial dysfunction, and activation of apoptotic path as shown in Figure 15. At higher concentration, accumulation of NPs likely disrupts cellular metabolism and integrity, leading to enhanced cytotoxicity. Meanwhile, the negligible toxicity at lower concentrations highlights the anticancer potential of Fe doped CaONPs.

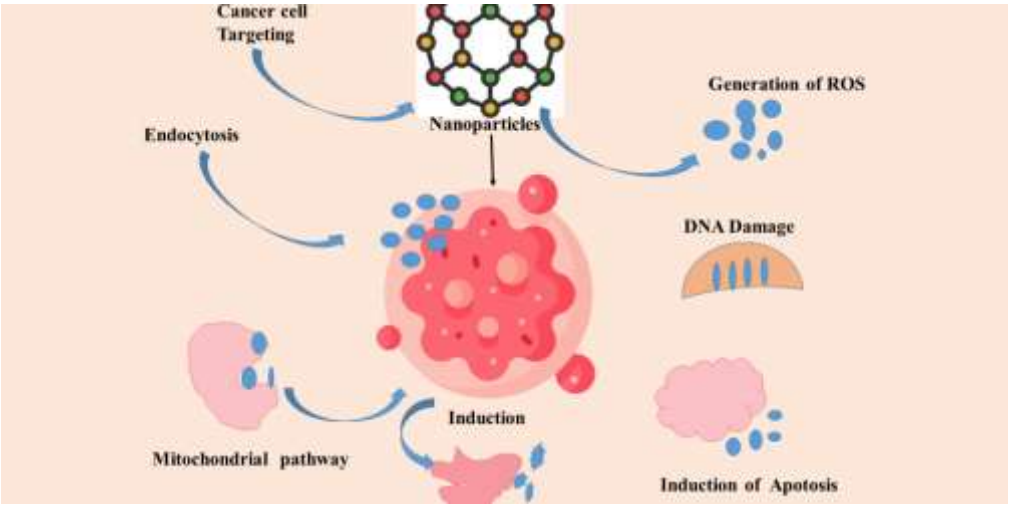

Figure 15. Mechanism of Anticancer potential

An evaluation of the anticancer potential of Fe doped CaONPs had been carried out on MCF-7 (breast cancer) cells using an MTT assay to determine their cytotoxicity at various concentrations between 0.78 - 100 µg/mL. The results in Figure 16. showed that increasing concentrations of CaONPs decreased cell viability in a concentration-dependent manner providing evidence of their potential ability to induce cytotoxicity.

The highest tested concentration of 100 µg/mL produced a significant reduction in cell viability to 22.91%, indicating that this dose has very high levels of cytotoxicity towards cancer cells. Similarly, a concentration of 50 µg/mL also produced a significant reduction in cell viability to 43.28%, thus confirming that at this level, there is substantial inhibition of cancer cell growth. Lower concentrations of 25 µg/mL and 12.5 µg/mL produced higher cell viability values of 84.28% and 87.64% respectively. Very low doses such as 1.56 and 0.78 µg/mL showed very little, if any, effect on cell viability as cell viability was close to or greater than 100%. Therefore, these concentrations can be considered to have very little toxic effects on the cells and are therefore expected to exert little toxicity when used for treatment of cancer.

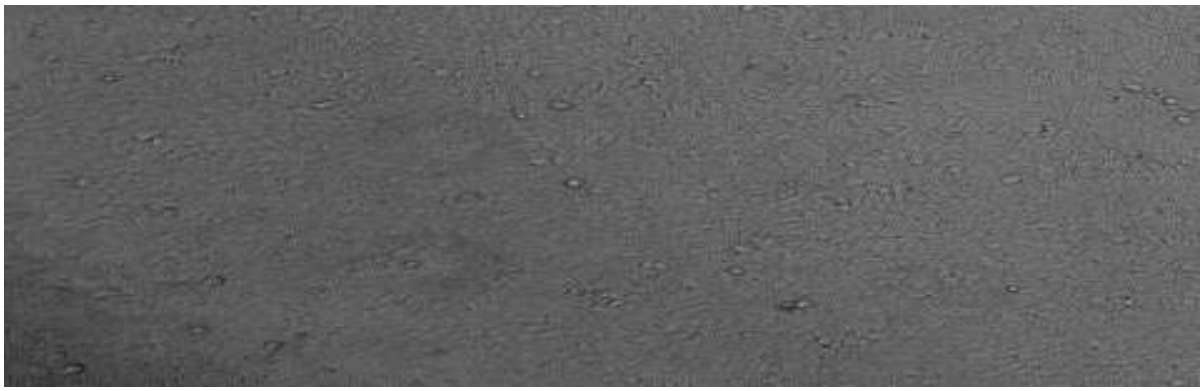

(a)Cancer cell without treatment

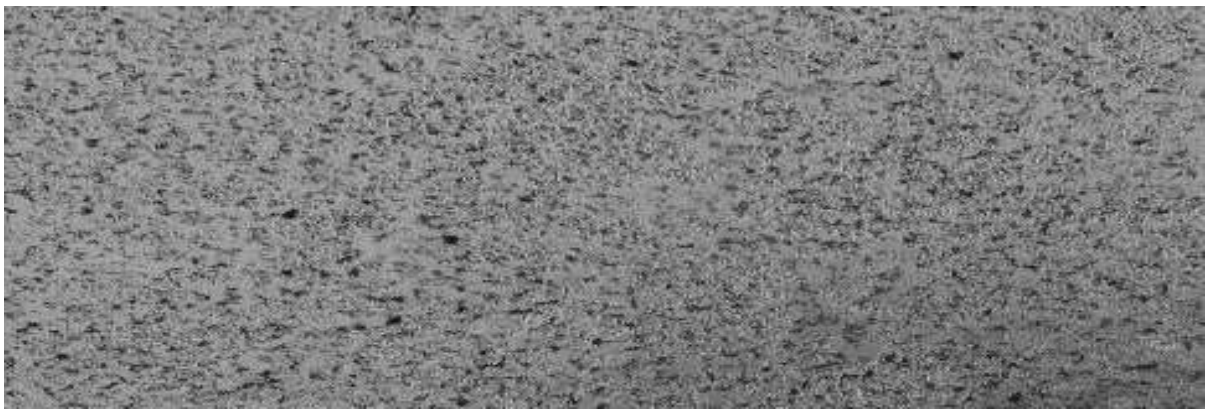

(b) low cell density (treated by Fe doped CaONPs)

Figure 16. Reduced cancer cell growth by Fe doped CaONPs.

The logarithmic regression analysis curve in Figure 17. Shown that there was a very strong relationship between the nanoparticle's concentration and reduced cells with an R^2 value of 0.8175. The calculated concentration of Fe-doped CaONPs that would kill 50% (IC_{50}) of the cells was about 54 µg/mL.

This means that these NPs may provide moderate to strong anti-cancer effects. The mechanism of cancer cell death is consistent with that reported for other metal oxide NPs. These NPs usually create reactive oxygen species (ROS), which

creates oxidative stress, causes the mitochondria not to work correctly, and activates the pathway to cause the cell to die. At higher concentrations, there is more of the nanoparticle, and they can disrupt cellular metabolism and the cell's integrity. Ultimately both events lead to cancer cell death. Hence, The findings suggest that Fe doped CaONPs possess significant dose dependent anticancer effects.

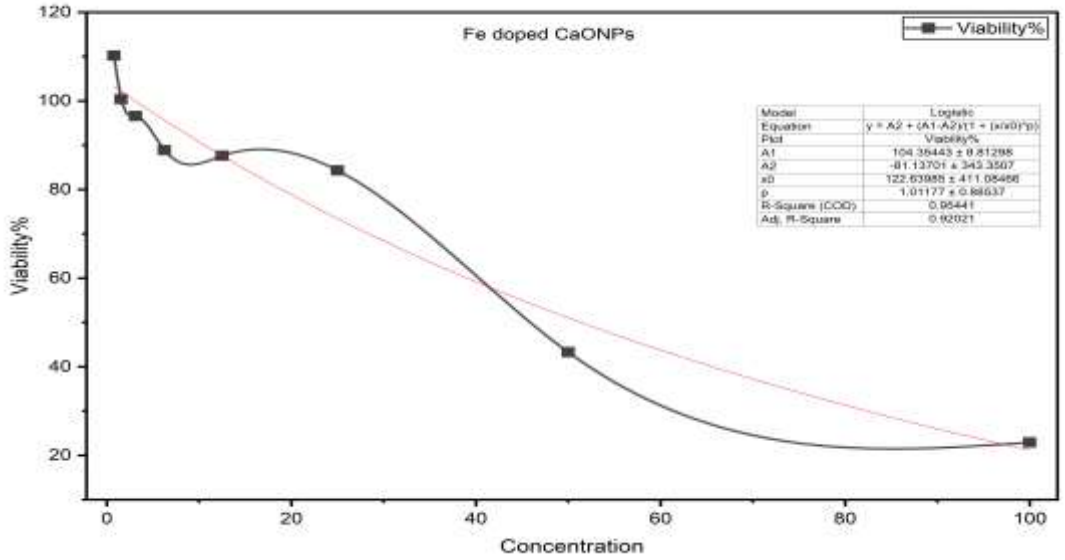

Figure 17. Concentration dependent reduction in cancer cell viability by Fe doped CaONPs.

These findings suggest that Fe doped CaONPs possess promising anticancer activity, with selective cytotoxicity against cancer cell at higher doses and minimal at lower concentration. This dual behaviour is advantageous for developing nanoparticle based therapeutic approaches, through further mechanistic and in-vivo studies are required to confirm their potential.

CONCLUSION

This investigation successfully demonstrates the green synthesis of CaONPs, α-Fe_2O_3NPs and Fe doped CaONPs using Aegle marmelos leaf extract as natural reducing and stabilizing agent. The green approach eliminates the use of toxic chemicals, reduces the environmental hazards, and aligns with the principle of green chemistry and sustainable development. The characterization results obtained through UV-Visible spectroscopy, FT-IR, XRD, SEM and EDX confirmed the formation of crystalline, pure NPs with nanoscale morphology and elemental homogeneity. The presence of bioactive phytochemicals in plant extract facilitates reduction and stabilization process.

Photocatalytic study reveals that all three NPs exhibited dye degradation efficiencies, with Fe doped CaONPs showing superior of degradation efficiency compared to both of CaONPs and α-Fe_2O_3NPs. The enhanced photocatalytic activity of Fe doped CaONPs can be attributed to improved charge separation and extended light absorption into the visible region upon iron doping. Notably, Fe doped CaONPs achieved 82.58%, 61.80% and 83.63% degradation efficiency for Reactive Red, Reactive Blue and real sample of textile wastewater respectively under combined solar irradiation and Sonicator treatment. Kinetic studies further confirmed pseudo-first-order behaviour, with Fe doped CaONPs exhibiting highest rate constant, making them reliable for wastewater treatment.

In addition to environmental remediation, the green synthesized NPs demonstrated strong antimicrobial potential. Fe doped CaONPs creates largest inhibition zones against including Micrococcus luteus, Bacillus cereus and bacillus megaterium confirming that iron doping significantly enhanced antibacterial activity. This dual functionality emphasizes their applicability in disinfection processes and biomedical sectors.

This anticancer evaluation of Fe doped CaONPs further highlighted their therapeutic applications. A clear dose dependent cytotoxic effect was observed, with cell viability reduced to approximately 22% at 100 µg/mL concentration and an IC50 value of approximately 54 µg/mL. The cytotoxic effect mediated by ROS generation, mitochondrial dysfunction and apoptosis in cancer cell. Essentially, negligible toxicity at lower concentrations shows good

This study demonstrates that green synthesized CaONPs, α-Fe_2O_3NPs and Fe doped CaONPs are multifunction nanomaterials with potential applications in wastewater treatment, antimicrobial and cancer therapy. Their cost-effective and eco-friendly synthesis method, combined with broad-spectrum activity, suggests them as alternative to conventional chemical synthesis methods. Thus, this work contributes significantly to the field of sustainable nanotechnology, offering an integrated solution links environmental remediation and biomedical applications.

Acknowledgements

The authors are thankful to the Department of Chemistry, Ganpat University, Kherva, Mehsana and Department of Chemistry, Indus institute of Sciences, Indus University, Ahmedabad for providing necessary facilities and guidance to carry out the work.

Funding statement

This research received no specific grant from any funding agency in the public, commercial, or not-for-profit sectors.

Conflict of Interests
The authors declare no conflict of interest.

REFERENCES

[1] E. Garcia, "The Essential Role of Water: A Critical Resource for Life and Sustainability," 8, (2024): 2581. 10.21767/2581-804X-8.3.27.
[2] N. Zhen, I. Rutherfurd, M. Webber, "Ecological water, a new focus of China's water management," Science of the Total Environment 879, (2023): 163001. https://doi.org/10.1016/j.scitotenv.2023.163001.
[3] Deeksha, A. K. Shukla, "Ecosystem Services: A Systematic Literature Review and Future Dimension in Freshwater Ecosystems," Applied Sciences 12, (2022): 8518. https://doi.org/10.3390/app12178518.
[4] Z. Liu et al., "Scarcity and quality risks for future global urban water supply," Landscape Ecology 39, (2024): 1–17. https://doi.org/10.1007/s10980-024-01832-0.
[5] A. P. Onyena, K. Sam, "The blue revolution: sustainable water management for a thirsty world," Discover Sustainability 6, (2025). https://doi.org/10.1007/s43621-024-00631-6.
[6] B. S. Rathi, P. S. Kumar, D. V. N. Vo, "Critical review on hazardous pollutants in water environment," Science of the Total Environment 797, (2021): 149134. https://doi.org/10.1016/j.scitotenv.2021.149134.
[7] I. Manisalidis et al., "Environmental and health impacts of air pollution," Frontiers in Public Health 8, (2020): 1–13. https://doi.org/10.3389/fpubh.2020.00014.
[8] L. Lin, H. Yang, X. Xu, "Effects of water pollution on human health," Frontiers in Environmental Science 10, (2022). https://doi.org/10.3389/fenvs.2022.880246.
[9] S. Singh, R. Jayaram, "Attainment of water and sanitation goals," Sustainable Water Resources Management 8, (2022): 1–15. https://doi.org/10.1007/s40899-022-00719-9.
[10] J. Evaristo et al., "Water woes: institutional challenges in achieving SDG 6," Sustainable Earth Reviews 6, (2023). https://doi.org/10.1186/s42055-023-00067-2.
[11] S. Biswas et al., "India's achievement towards SDG 6," BMC Public Health 22, (2022): 1–16. https://doi.org/10.1186/s12889-022-14316-0.
[12] L. Crockford, "Achieving cleaner water for SDG 6," Frontiers in Environmental Science 10, (2022): 1–7. https://doi.org/10.3389/fenvs.2022.976687.
[13] United Nations et al., "Progress on wastewater treatment," (2024).
[14] A. Haider et al., "Green synthesized nickel oxide nanoparticles," Nanoscale Research Letters 15, (2020). https://doi.org/10.1186/s11671-020-3283-5.
[15] J. Tripathy et al., "Advances in nanoparticles for water treatment," Water 16, (2024): 1–26. https://doi.org/10.3390/w16111481.
[16] F. Khan et al., "Green nanotechnology: plant-mediated nanoparticle synthesis," Nanomaterials 12, (2022). https://doi.org/10.3390/nano12040673.
[17] P. N. Silva-Holguín et al., "Silver nanoparticles in water remediation," Materials 17, (2024). https://doi.org/10.3390/ma17091939.
[18] K. K. Singh, A. Singh, S. Rai, "Nanomaterials for water purification," Materials Today Proceedings 51, (2021): 1157–1163. https://doi.org/10.1016/j.matpr.2021.07.116.
[19] A. B. Patil et al., "Green synthesis of CuO nanoparticles using Aegle marmelos," RSC Advances 15, (2025): 44061–44070. https://doi.org/10.1039/D5RA07029E.
[20] P. Rama et al., "Green synthesis of silver nanoparticles from Aegle marmelos leaf extract," Heliyon 9, (2023): e16277. https://doi.org/10.1016/j.heliyon.2023.e16277
[21] V. Jadhav et al., "CaO nanocomposites cytotoxic and antifungal activity," Discover Nano 20, (2025). https://doi.org/10.1186/s11671-025-04322-7.
[22] J. Zúñiga-Miranda et al., "Iron oxide nanoparticles: green synthesis and antimicrobial activity," Nanomaterials 13, (2023): 1–35. https://doi.org/10.3390/nano13222919.
[23] M. H. Meshkatalsadat, M. Solaimani, "Eco-friendly synthesis of calcium oxide nanoparticles," International Journal of New Chemistry 10, (2023): 27–34.
[24] W. C. Ulakpa et al., "Synthesis of CaO nanoparticles from snail shells," Journal of Turkish Chemical Society A 11, (2024): 825–834. https://doi.org/10.18596/jotcsa.1416214.
[25] N. O. Eddy et al., "Synthesis and characterization of CaO nanoparticles from periwinkle shells for the treatment of tetracycline-contaminated water by adsorption and photocatalyzed degradation," Results in Engineering 24, (2024): 103374. https://doi.org/10.1016/j.rineng.2024.103374.
[26] H. Sridevi, M. R. Bhat, P. S. Kumar, N. M. Kumar, R. Selvaraj, "Structural characterization of cuboidal α-Fe_2O_3 nanoparticles synthesized by a facile approach," Applied Nanoscience 13, (2023): 5605–5613. https://doi.org/10.1007/s13204-023-02780-y.
[27] P. N. V. K. Pallela et al., "Antibacterial efficacy of green synthesized α-Fe_2O_3 nanoparticles using Sida cordifolia extract," Heliyon 5, (2019): e02765. https://doi.org/10.1016/j.heliyon.2019.e02765.
[28] N. Bashir, S. Gulzar, S. Shad, "Green synthesis of silver and iron nanocomposites for dye removal," Frontiers in Toxicology 6, (2024): 1–9. https://doi.org/10.3389/ftox.2024.1288783.
[29] R. Selvaraj et al., "Magnetic α-Fe_2O_3 nanospheres for Fenton-like degradation of crystal violet dye," Applied Nanoscience 11, (2021): 2227–2234. https://doi.org/10.1007/s13204-021-01952-y.
[30] H. J. Fatih, M. Ashengroph, A. Sharifi, "Potent antibacterial, anti-biofilm and anti-virulence agent against pathogenic bacteria," BMC Microbiology 24, (2024): 1–13. https://doi.org/10.1186/s12866-024-03699-2.

[31] H. Hemmami et al., “Green synthesis of CaO nanoparticles from eggshells and heavy metal adsorption,” Frontiers in Environmental Science 12, (2024): 1–17. https://doi.org/10.3389/fenvs.2024.1450485.
[32] P. Rama et al., “Green synthesis of silver nanoparticles from Aegle marmelos leaf extract,” Heliyon 9, (2023): e16277. https://doi.org/10.1016/j.heliyon.2023.e16277.
[33] S. Patil, R. Venckatesh, R. Seenivasan, “Green synthesis of silver nanoparticles using Aegle marmelos leaf extract,” International Journal of Pharmacy and Pharmaceutical Sciences 7, (2015): 169–173.
[34] R. Eram et al., “Biocompatibility of green synthesized CaO nanoparticles with Danio rerio,” Journal of Nanotheranostics 2, (2021): 51–62. https://doi.org/ 10.3390/jnt2010004.
[35] R. Koley, N. K. Mondal, “Calcium-based nanofertilizer and fluoride uptake reduction in rice,” Plant Nano Biology 9, (2024): 100087. https://doi.org/10.1016/j.plana.2024.100087.
[36] T. S. S. K. Naik et al., “Green synthesis of CaO nanoparticles for electrochemical urea detection,” Scientific Reports 13, (2023): 1–9. https://doi.org/10.1038/s41598-023-46728-2.
[37] A. Hussain et al., “Synthesis, characterization and applications of iron oxide nanoparticles,” 17, (2023).
[38] B. Ahmmad et al., “Mesoporous hematite nanoparticles and photocatalytic activity,” Advanced Powder Technology 24, (2013): 160–167. https://doi.org/10.1016/j.apt.2012.04.005.
[39] N. Ndou et al., “Green synthesis of hematite nanoparticles and plant growth effects,” Plants 12, (2023): 1–23. https://doi.org/10.3390/plants12071425.
[40] S. Mizuno, H. Yao, “Electronic transitions of α-Fe_2O_3 nanoparticles,” Journal of Magnetism and Magnetic Materials 517, (2021): 167389. https://doi.org/10.1016/j.jmmm.2020.167389.
[41] M. Ikram et al., “Enhanced photocatalytic degradation using CaO nanorods,” ACS Omega 7, (2022): 27503–27515. https://doi.org/10.1021/acsomega.2c02732.
[42] M. F. Al-Hakkani, G. A. Gouda, S. H. A. Hassan, “Review of green synthesis of hematite nanoparticles,” Heliyon 7, (2021): e05806. https://doi.org/10.1016/j.heliyon.2020.e05806.
[43] Y. G. Habba, M. Capochichi-Gnambodoe, Y. Leprince-Wang, “Iron-doped ZnO nanowires for water purification,” Applied Sciences 7, (2017). https://doi.org/10.3390/app7111185.
[44] M. Mazher et al., “Biosynthesis of CaO nanoparticles and bioactivities,” Materials 16, (2023): 1–21. https://doi.org/10.3390/ma16072768.
[45] G. Nasir et al., “CaO nanoparticles for Rhodamine B degradation,” Scientific Reports 14, (2024): 1–24. https://doi.org/10.1038/s41598-024-71172-1.
[46] S. J. Kashyap, R. Sankannavar, G. M. Madhu, “Fe_2O_3 nanoparticles via solution combustion,” Materials Chemistry and Physics 286, (2022): 126118. https://doi.org/10.1016/j.matchemphys.2022.126118.
[47] D. M. S. N. Dissanayake et al., “Hematite nanoparticles for dye adsorption,” RSC Advances 9, (2019): 21249–21257. https://doi.org/10.1039/c9ra03756j.
[48] N. Nami, A. S. Bostanabad, “Fe_3O_4/CaO nanoparticles and catalytic properties,” Journal of Nanostructures 12, (2022): 160–169. https://doi.org/10.22052/JNS.2022.01.015.
[49] B. J. Madhu et al., “CaO nanoparticles from eggshells: structural and catalytic behavior,” SN Applied Sciences 3, (2021). https://doi.org/10.1007/s42452-021-04607-3.
[50] L. G et al., “Green-derived CaO nanoparticles for biomedical applications,” Results in Engineering 27, (2025): 105815. https://doi.org/10.1016/j.rineng.2025.105815.
[51] J. Jeevanandam et al., “Metal-doped MgO nanoparticles for enzyme inhibition,” Materials Today Bio 31, (2025): 101520. https://doi.org/10.1016/j.mtbio.2025.101520.
[52] C. D. Powell et al., “Nano-structural effects on hematite nanoparticle heating,” Nano Convergence 8, (2021). https://doi.org/10.1186/s40580-021-00258-7.
[53] A. Sajjad et al., “Fabrication of hematite nanoparticles under spectral light,” Nano Trends 2, (2023): 100010. https://doi.org/10.1016/j.nwnano.2023.100010.
[54] M. Hanif et al., “Magnetic CaO/Fe_2O_3 catalysts for biodiesel production,” Catalysts 13, (2023): 1–14. https://doi.org/10.3390/catal13060998.
[55] O. Reyes-Vallejo et al., “CaO–Fe_3O_4 composites for dye degradation,” Environmental Science and Pollution Research 32, (2025): 9901–9925. https://doi.org/10.1007/s11356-025-36310-w.
[56] G. Yang et al., “Particle size and ultrasonic treatment in nanoparticle synthesis,” Ultrasonics Sonochemistry 73, (2021): 105497. https://doi.org/10.1016/j.ultsonch.2021.105497.
[57] M. K. Hossain, M. M. Hossain, S. Akhtar, “TiO_2 and Cr-doped TiO_2 for chlorophenol degradation,” ACS Omega 8, (2023): 1979–1988. https://doi.org/10.1021/ACSOMEGA.2C05107.
[58] U. O. Aigbe, O. A. Osibote, “Green synthesis of metal oxide nanoparticles,” Journal of Hazardous Materials Advances 13, (2024): 100401. 1 https://doi.org/0.1016/j.hazadv.2024.100401.
[59] K. Povija et al., “Photocatalytic degradation of acetamiprid,” Catalysis Communications 169, (2022): 1–7. https://doi.org/10.1016/j.catcom.2022.106474.
[60] G. E. Lau et al., “Eco-friendly photocatalysts for dye degradation.”
[61] J. Zhong et al., “Photo-Fenton removal of textile dye wastewater,” Water 13, (2021). https://doi.org/10.3390/w13070968.
[62] G. Jalloul et al., “Fe-sensitized TiO_2 for tetracycline degradation,” Frontiers in Environmental Science 10, (2022): 1–13. https://doi.org/10.3389/fenvs.2022.873257.
[63] G. Wang, H. Cheng, “Photocatalysis and sonocatalysis for dye wastewater treatment,” (2023).
[64] B. M. Quy et al., “Photocatalytic materials study,” RSC Advances (2025): 1590–1603. https://doi.org/10.1039/d4ra08262a.

[65] N. Mammari et al., “Oxidative stress-mediated antimicrobial properties of metal nanoparticles,” Microorganisms 10, (2022): 1–20. https://doi.org/10.3390/microorganisms10020437.